

REVERSE BALLISTIC IMPACT STUDIES OF THIN PLATE PERFORATION

L.C. F o r d e^{1,2)}, W.G. P r o u d¹⁾, S.M. W a l l e y¹⁾,
P.D. C h u r c h³⁾, R. C o r n i s h³⁾

¹⁾ **Fracture and Shock Physics Group**
Cavendish Laboratory

J.J. Thomson Avenue, Cambridge CB3 0HE, United Kingdom

²⁾ **Measurement Standards Laboratory**
New Zealand

³⁾ **QinetiQ**
Fort Halstead
Sevenoaks, Kent TN14 7BP

Full-scale ballistic experiments using tungsten rods and rolled homogeneous armour (RHA) steel plates are expensive to perform. For this reason, a study has been performed into the possibility of using less expensive, more easily available metals in small-scale laboratory experiments. The metal pairs chosen listed in order as armour/penetrator materials were: RHA steel/tungsten, dural/mild steel, and copper/aluminium. In order to be able to use as many diagnostics as possible (including high speed photography, VISAR, stress gauges) the reverse ballistic configuration was used. This configuration also allowed the determination of the high rate, low strain mechanical properties of mild steel to be determined. Finally, a comparison was made between experiment and numerical predictions made using a modified Armstrong-Zerilli constitutive model for the RHA steel/tungsten pair. The model was found to underpredict the penetration, probably because failure mechanisms were not incorporated.

1. INTRODUCTION

1.1. Background to this study

A vast literature with a long history exists on the subject of terminal ballistics, and publications in this area show no sign of slowing, particularly with the recent improvements in hydrocode modelling.

The experimental data obtained in the field of terminal ballistics generally consists of the following parameters:

- (i) velocity and trajectory of projectile prior to impact,
- (ii) velocity and trajectory of projectile after impact,
- (iii) masses, velocities and trajectories of fragments generated by the impact process,
- (iv) motion imparted to the target,
- (v) hole size in and mass loss from the target,
- (vi) shape and dimensions of the recovered projectile.

From these observations the nature of the penetration mechanisms and projectile deformation can be inferred. These can be plotted as a mechanism map [1] in a manner similar to Ashby deformation maps [2]. The ballistic limit velocity (i.e., that required for perforation) may also be determined from such experiments. Penetration mechanics is complicated when the deformation due to impact includes the rear surface of the target [3].

1.2. Methods of study

Because we wished to use as many diagnostics as possible in order to constrain and exercise material constitutive models, we decided to perform reverse ballistics studies on instrumented rods. Despite its many advantages in terms of ease of instrumentation, the reverse ballistic configuration has a number of drawbacks, including limitations on (i) the diameter of the target to that of the available gun barrel, and (ii) the mass of the target (the heavier the target the slower it can be fired). Also the movement of the target plate across the field of view inevitably creates parallax.

The technique we used in all the experiments reported here was high-speed photography. As debris clouds and fracture can obscure the target to optical photography, we also performed single-frame X-ray flash radiography (sometimes combined with speckle analysis). These studies have been reported elsewhere [4, 5].

Instrumentation of reverse ballistic impacts by, for example, foil stress gauges permits the acquisition of a force history [6]. Stress histories may also be recorded using VISAR (Velocity Interferometer System for Any Reflector), a laser interferometer system that measures the particle velocity produced by an in-material stress pulse incident on a free surface [7]. Depending on the application, this may be more convenient than embedded foil gauges. We used both techniques in this study.

1.3. Why perform model ballistic experiments?

Penetration models are necessary in the development of both armour and projectiles. In seeking to conduct experiments to enhance understanding, the

designers of projectiles or targets can change: (a) the configuration, e.g., plate thickness, plate spacing, reactive armour, projectile length, projectile nose shape, segmentation of rod; (b) the material, e.g., ductility, toughness, yield strength; and (c) the magnitude and direction of motion.

For example, some strategies used to protect a space include:

- (i) deflecting the penetrator by angling the armour [8, 9] (this also has the effect of increasing the target thickness along the projectile trajectory);
- (ii) fracturing or eroding the penetrator by (a) placing very hard ceramic plates at the front [10] or (b) moving the front plate very fast across the projectile trajectory using explosives (reactive armour) [11];
- (iii) dispersing the rod fragments by spacing the target plates [12–14].

Attempts to counter these strategies include:

- (i) increasing the penetrator length so that a sufficient length remains after erosion to perforate the target [15];
- (ii) designing the penetrator so that different sections have different properties [16], e.g., making the nose hard, dense and blunt so as to load the target as severely as possible on impact while making the rear more ductile to reduce the likelihood of fragmentation due to bending stresses;
- (iii) increasing the impact velocity so as to stress the target more severely [17].

The wide variety of types of ballistic impact means that there is no optimum configuration of materials to suit all situations [18]. Hence, the best armour design for defeating shaped-charge jets will probably not be the most efficient at resisting long rod penetrators [19, 20].

Experimental testing can be performed in three different ways:

- (i) full-scale – this is expensive and not ideal for exploring a large set of experimental parameters. The diagnostics that can be deployed may also be limited on an outside range;
- (ii) small-scale – the main advantages being that fabrication, machining and assembly of equipment are much easier on a small scale. Experiments are also easier to perform within a laboratory where the experimental parameters can be more easily explored and a wide range of diagnostics used. The main disadvantage is that scaling up to full-scale may not be straightforward [21, 22];
- (iii) material property testing – since the penetration process takes place in several different phases [23–25], experiments characterising the material response to each of the various different modes of loading (e.g., shock propagation, adiabatic shear, dynamic fracture) need to be carried out. Such experiments should be compared with appropriate constitutive models using numerical modelling.

2. EXPERIMENTAL

The experiments reported in this paper consisted of impacts between long rods and thin metal plates. Such plates allow the behaviour of the rear face of the target to be observed using high-speed photography, but other aspects of penetration (such as ricochet, ballistic limits, rod erosion and the influence of the length/diameter (L/D) ratio on penetration depth) cannot be studied. Also deformation of a thin plate is restricted to a small region surrounding the impact point. The holes formed in the plates were found to be cylindrical and to have contracted after impact as rods recovered after impact were unable to fit through them.

The aspect ratio of the rods studied ($L/D \geq 10$) was determined by the requirement to be able to instrument them with stress gauges. Previous studies have shown that gauges should be placed at least ten diameters from the impact end to improve the approximation to uniaxial stress conditions [26, 27]. In order to instrument the rods, the target had to be fired at the rods (reverse ballistics) [28] (see Fig. 1). The gun used was primarily built for plate impact studies [29].

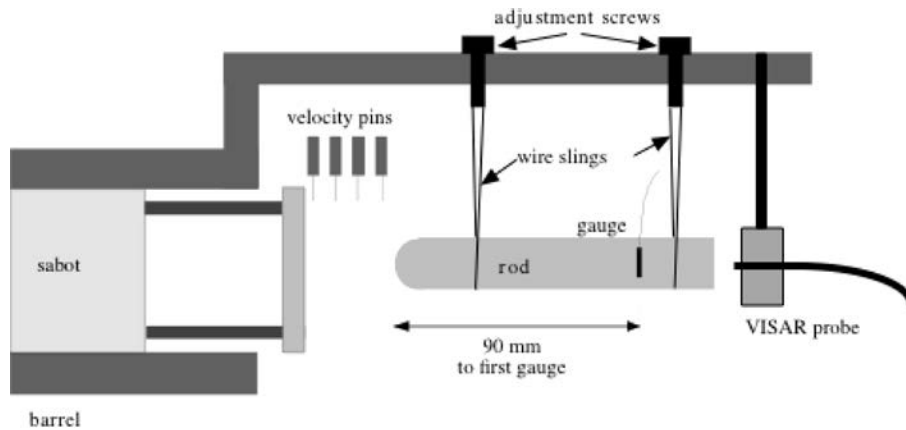


FIG. 1. Schematic diagram of the reverse ballistic set-up used in these experiments [28].

Annealed copper and tungsten alloy rods with hemispherical ends and with diameter 10 mm and length 100 mm were supplied by QinetiQ. 9.5 mm diameter mild steel rods were sourced locally and typically used in lengths of 215 mm (or occasionally 340 mm) with either hemispherical or flat ends. The properties of all the materials used are listed in Table 1. Pure aluminium and RHA steel plates were supplied by QinetiQ for impact by the copper and tungsten alloy rods respectively, whereas a work-hardened aluminium alloy (dural) was used with the mild steel rods. The ratios of the rod-to-plate densities and rod-to-plate yield strengths are given in Table 2.

Table 1. Properties of the materials used in these experiments.

	Tungsten alloy (Densimet 176 FNC)	Pure copper (XM C103)	Mild steel (EN3B)	Dural (AA6082-T6) fully hardened	Rolled Homogeneous Armour (RHA) Steel (UK 100)
Chemical composition [wt. %]	W: 92.3, Ni: 4.92, Fe: 1.45, Co: 1.40		Fe: 98.9, Cu: 0.2, Mn: 0.9		
Density $\tilde{\rho}$ [kg m ⁻³]	17560 ± 20	8924 ± 1	7818 ± 6	2703 ± 5	7824 ± 5
Longitudinal elastic wave speed c_L [m s ⁻¹]	5190 ± 5	4760 ± 5	5913 ± 5	6400 ± 5	5905 ± 5
Transverse elastic wave speed c_T [m s ⁻¹]	2850 ± 5	2330 ± 5	3248 ± 2	3150 ± 5	3239 ± 5
Rod elastic wave speed c_R [m s ⁻¹]	4570 ± 20	3820 ± 20	5200 ± 10	5160 ± 20	5190 ± 30
Bulk elastic wave c_B [m s ⁻¹]	4010 ± 10	3930 ± 10	4571 ± 8	5270 ± 10	4570 ± 10
Young's modulus E [GPa]	366 ± 2	130.1 ± 0.7	211.8 ± 0.6	71.9 ± 0.3	211 ± 1
Shear modulus μ [GPa]	142.6 ± 0.4	48.5 ± 0.1	82.5 ± 0.1	26.82 ± 0.08	82.1 ± 0.2
Bulk modulus K [GPa]	283 ± 1	137.6 ± 0.5	163.4 ± 0.5	75.0 ± 0.2	163.4 ± 0.6
Poisson's ratio ν	0.284 ± 0.006	0.342 ± 0.006	0.284 ± 0.004	0.340 ± 0.005	0.285 ± 0.006
Dynamic yield stress σ_y [GPa]	2.05 ± 0.1	0.4 ± 0.1	0.93 ± 0.02	0.30 ± 0.05	1.44 ± 0.05

Notes on the provenance of this data: The yield stresses of all materials were measured in-house using a split Hopkinson pressure bar. The longitudinal and transverse sound speeds as well the density and yield stress were measured in-house for all the materials except copper, the data for which were obtained from the LASL Shock Hugoniot Data Book [30]. Other properties that depend on these were calculated.

Table 2. Ratios of properties of rods to properties of plates.

Plate/rod pairs	Rod density/plate density	Rod yield stress/plate yield stress
Pure aluminium/copper	3.3	2.1
RHA steel/tungsten alloy	2.2	1.4
Dural/mild steel	2.9	3.2

A consequence of the rod lengths chosen was that the time taken for an elastic wave to travel to the far end of the rod and return was often long compared to the duration of the high-speed photographic sequences taken. This meant that the nose of the rod remained nearly stationary during photographic observation except for when significant plastic deformation (shortening) occurred in the rod.

As the diameter of the gun barrel used is 50 mm the rod diameter needed to be significantly less than this so as to reduce edge effects during impact. The minimum time before the edge of the metal target plate could have an influence is the time for an elastic wave to travel from its centre out to the mounting pillars and back (a distance of about 20 mm; see Fig. 2), i.e., around 6 μ s. The diameter of the rods also needed to be larger than the stress gauges used (*ca.* 3 mm) and to be large enough to give reasonable photographic resolution. A diameter of 10 mm was settled on as meeting these various requirements.

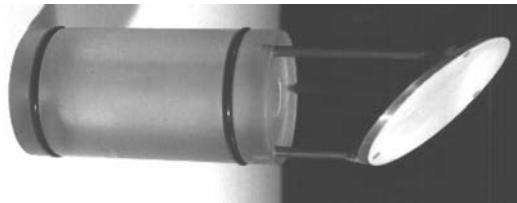


FIG. 2. Photograph of a 3 mm thick plate mounted at 45° on the front of a 50 mm diameter polycarbonate sabot.

The parameters investigated were: velocity, plate thickness, angle of impact, nose shape, and material. The choice of materials was influenced by the desire to observe the effect of a range of properties (ductility, density, work-hardening) while also trying to keep the ratio of the projectile/target properties as close as possible to that of tungsten/RHA armour steel. This led to the choice of the following pairs: annealed copper with annealed aluminium, mild steel and work-hardened dural, tungsten/RHA steel. For these pairs, the ratio of rod density to plate density varied between 2.2 and 3.5 and the ratio of yield strengths varied between 1.4 and 3.2 (see Tables 1 and 2). These combinations ensured a variety of perforation mechanisms could be observed.

The plates were thin enough that their rear surface exerted a mechanical influence for most of the perforation process. Specifically, the thicknesses of the

aluminium plates used were 5 mm and 10 mm, the RHA plates 5 mm, and the dural plates 3, 6 and 10 mm. The plates were mounted at three different angles to the rod axis (90° , 45° and 30°) onto a polycarbonate sabot using three slender steel pillars near the edges (Fig. 2). The plates were glued onto the pillars with metal-filled epoxy. The centre of the forward-facing face of the sabot was recessed to reduce post-impact damage.

All the high-speed sequences were taken using an FS501 Ultramac camera using back illumination from a flash tube. There are a number of issues to be considered in the interpretation of the sequences. First, the motion of the plate in the field of view means that the viewing angle changes (parallax). Also because the images were taken in silhouette, the front and back surfaces were not illuminated and thus the plate appears to change thickness during the sequence (compare the beginning and end of the sequence shown in Fig. 3). This reduces

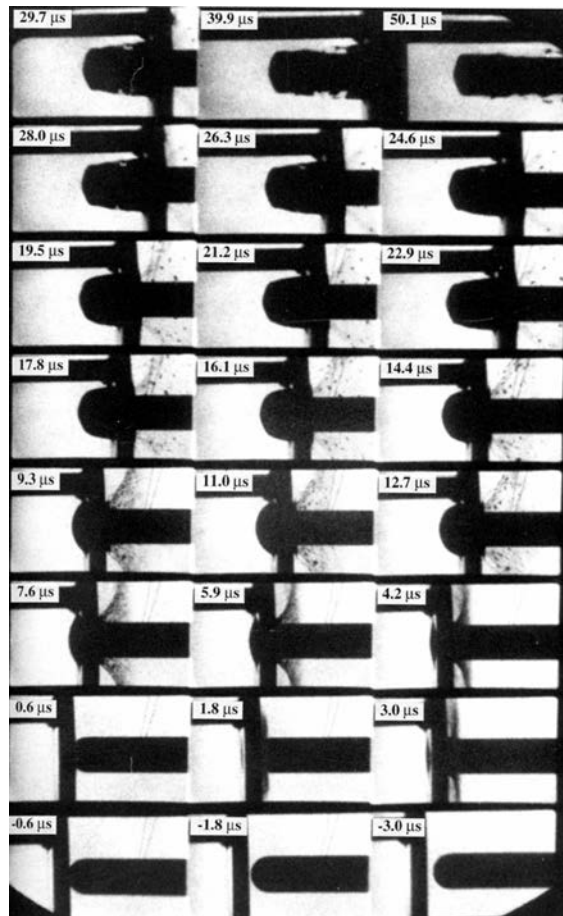


FIG. 3. High speed photographic sequence of reverse ballistic normal impact of a round nosed copper rod by a 4.8 mm thick annealed aluminium plate at 855 m s^{-1} .

the measurement accuracy of times when events take place. The rod diameter is, however, a reliable alternative distance scale marker. Second, for angled impact, any rotation of the plate during launch also obscures events on the surface. However, sabot rotation was never found to amount to more than 8° , and was usually much less. Third, because a dove prism was used to rotate the image by 90° so as to make best use of the frames output by the camera, shear distortion was introduced into the photographs. This distortion can make a plate oriented at 90° to the rod appear to be slightly angled (see, for example, Fig. 5).

3. IMPACT PHENOMENOLOGY

3.1. Characteristic times

The thickness of the plate determines, among other things, the fraction of the perforation time before the rod is significantly affected by the rear free surface. The effects of the relative dimensions of the plate thickness and nose radius may be characterised by comparing the time when the nose of the rod reaches a certain location with the time it would take to reach the same place if the plate were not present (see Fig. 4). It is best to think of this procedure as a guide to interpretation since errors are introduced into this scheme due to acceleration of the rod caused by the impact.

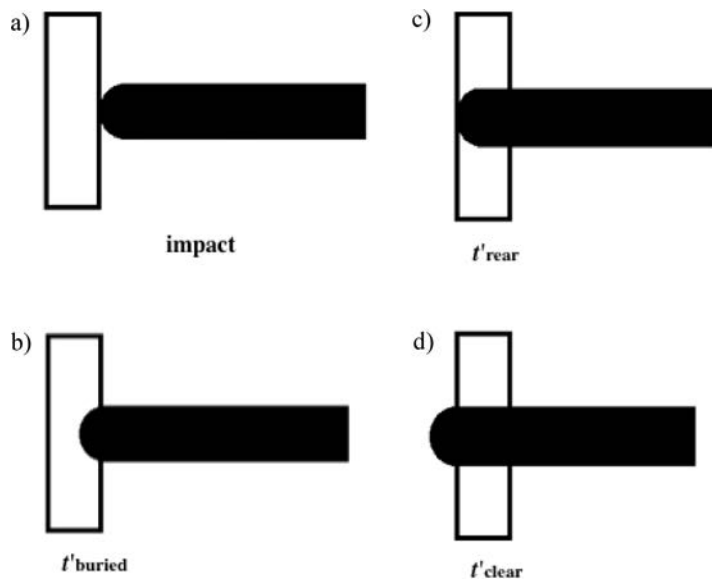


FIG. 4. Diagram illustrating the times after impact, calculated from the impact velocity and plate thickness, when the rod nose would (a) be just buried t'_{buried} (b) have just reached the rear surface t'_{rear} (c) have just cleared the rear surface of the plate t'_{clear} .

3.2. Round-nosed rods

The sequence of events typically seen in the normal impact of round-nosed rods are as follows: for the first microsecond or so, the load is applied over a small area which expands supersonically as more of the nose comes into contact with the plate surface [31–33]. This produces rapid radial flow of target material which jets laterally in a liquid-like manner (see Fig. 5). The geometry of the impact means that the angle of jetting changes continuously as the rod penetrates the plate. Thus the jets of material appear curved (Fig. 5d). Inspection of recovered rods showed that rod material did not form part of the ejecta for this material combination at this impact speed.

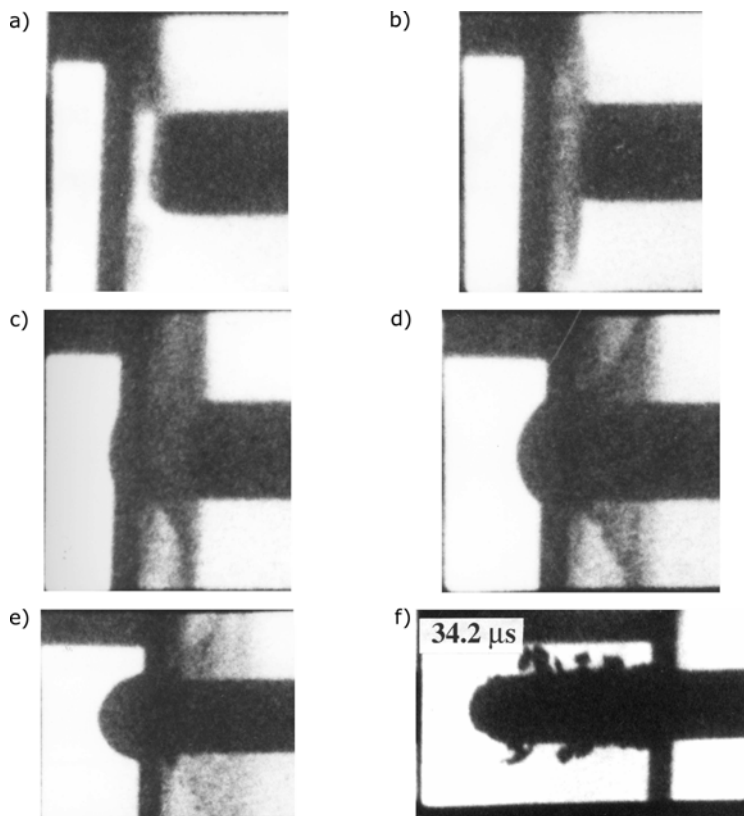


FIG. 5. Selected frames from the high-speed photographic sequence of the normal impact of a 9.5 mm diameter round-nosed mild steel rod by a 3 mm thick dural plate at 835 m s^{-1} : a) light flash seen $0.5 \mu\text{s}$ after impact; b) $1.7 \mu\text{s}$ after impact; c) $4.1 \mu\text{s}$ after impact; d) $6.5 \mu\text{s}$ after impact; e) $10.1 \mu\text{s}$ after impact; f) $34.2 \mu\text{s}$ after impact.

The rear surface of the plate will start to decelerate when the elastic stress wave generated by the impact first reflects off it. However, visible bulging does

not start until the plastic zone ahead of the rod reaches that surface (just before $1.8 \mu\text{s}$ in Fig. 3, for example). If the plate is sufficiently thin (as it is in the impact shown in Fig. 3) this will occur before the nose of the rod has fully penetrated the front surface. Plate material was pushed out by the rod eventually detaching as a plug attached to the front of the rod. A narrow shear zone is required for plugging, so plugging does not occur in metals which work-harden as this process suppresses the formation of adiabatic shear bands (ASBs) [34, 35]. Hence work-hardening materials flow uniformly to large strains. In these cases, a bulge forms whose diameter larger than the rod and which eventually tears away. This had certainly happened by $40 \mu\text{s}$ in Fig. 3.

Occasionally a brief flash of light was recorded at impact (Fig. 5a). The probable reason this was only rarely seen is that the duration of such flashes is substantially shorter than the interframe time of the camera, set to $0.3 \mu\text{s}$ in this case. Possible origins for these light flashes include: (i) the thermite reaction, if metals like copper and aluminium are used, or (ii) adiabatic compression of trapped gas between the surfaces [36]. As steel and aluminium were used in the experiment shown in Fig. 5, the latter explanation is more likely. In the sequence shown in Fig. 5, jets of material were visible by $1.7 \mu\text{s}$, reaching their final angle to the surface by $6.5 \mu\text{s}$ and beginning to die off by around $9 \mu\text{s}$. The bulge began to be visible around $3 \mu\text{s}$. The diameter of the bulge was nearly the same as the rod diameter, a characteristic of thin plates. The plate bulged out to a distance of three plate thicknesses before any notches appeared (the first sign of plug failure) at around $14 \mu\text{s}$. Subsequently, there were multiple failure points leading to the break-up of the plug into small pieces (Fig. 5f).

In a similar experiment performed on a 6 mm thick plate, the bulge appeared at around $7.0 \mu\text{s}$. This is a significantly smaller fraction of t'_{rear} than for the thinner plate ($7.0 \mu\text{s}$ is about 65% of $10.8 \mu\text{s}$ whereas $2.9 \mu\text{s}$ is 81% of $3.6 \mu\text{s}$). The thicker plate also bulged less (one plate thickness) before notches appeared.

3.3. Flat-ended rods

Figure 6 presents a typical high-speed sequence for normal impact on a flat-ended rod. The major difference with the hemispherical-nose rod case is that the full width of the rod enters the target on impact. This means there is little lateral displacement of plate material and no jetting. There is, however, intense shear around the circumference of the rod, increasing the likelihood of plug formation. During the breakout phase little lateral flow of the plug material would be expected (which causes plug thinning). The initial failure of the rear face favours pieces of target material around the rod circumference breaking away. This can be seen happening late on the sequence.

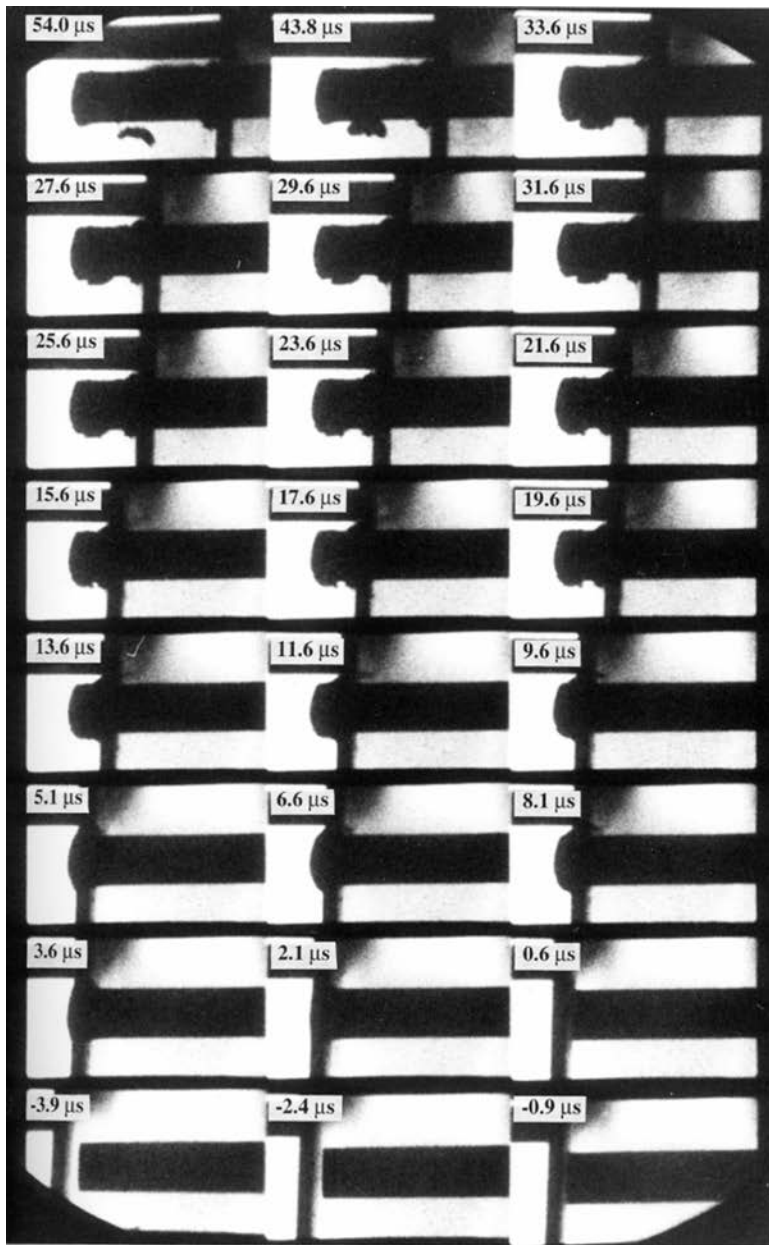


FIG. 6. High speed photographic sequence of the normal impact of a flat-ended mild steel rod by a 3.0 mm thick dural plate at 533 m s^{-1} .

Tables 3 and 4 present data obtained from high-speed photographic sequences of the normal impact of hemispherical and flat-ended steel rods struck by dural plates.

Table 3. Data obtained from high-speed photographic sequences for hemispherical-nosed steel rods struck normally by 3 mm thick dural plates.

Impact velocity [m s ⁻¹]	Time the plate first deviates from constant velocity [μs]	Time for rear of plate to become stationary [μs]	Time jets appear [μs]	Time rear bulge appears [μs]	Time rear notch appears [μs]	Extent of bulge at failure [%]*	Final plug thickness [mm]	t'_{rear} [μs]
556	2.4	21.6	3.6	3.6	16.8	300–400	0.8	5.4
561	2.0	9.2	3.2	3.2	15.2	≥ 300	1.3	5.3
549	2.4	4.8	2.4	2.4	13.2	300	1.7	5.5
543	2.3	10.2	1.7	2.9	12.5	≥ 300	1.6	5.5

* Note that '200%' means one extra plate thickness, '300%' two extra plate thicknesses and '400%' three extra plate thicknesses.

Table 4. Data obtained from high-speed photographic sequences for flat-ended mild steel rods struck normally by dural plates of various thicknesses.

Dural plate thickness [mm]	Impact speed [m s ⁻¹]	Time of first deviation from constant velocity [μs]	Time for rear of plate to become stationary [μs]	Time rear bulge appears [μs]	Time notch first appears in rear of plate [μs]	Extent of bulge at failure [%]	Final plug thickness [mm]	t'_{rear} [μs]
3	533	1.25	2.75	2.1	8.1	200	2.4	5.6
6	556	2.0	15.2	3.2	15.2	200	2.75	10.8
10	550	8.8	29.7	6.9	24.0	< 200	2.5	18.2

3.4. Oblique rod impacts

Oblique impact requires an extra characteristic time to describe it, i.e., where the centre of nose of the rod reaches the plate rear (see Fig. 7). The plate angle, plate thickness and nose radius determine the order the events identified in this figure occur in.

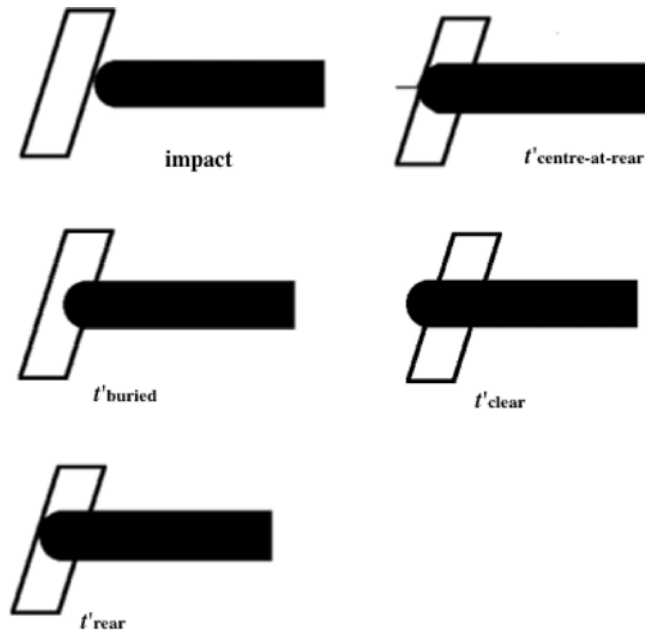


FIG. 7. Schematic diagram showing how the characteristic times are defined for oblique impact.

An angled plate has more resistance to penetration than the same plate oriented at 90° to the rod axis simply because of the greater thickness of material in the direction of motion. This concept may be quantified by the 'effective path length' (*EPL*) which is the distance that must be traversed by a rod through a plate before its nose is completely clear of the original rear surface. In normal impact of a hemispherical-nosed rod, the *EPL* will be the sum of the plate thickness and the rod radius. In angled impact, the width of the rod becomes important because the trailing edge of the nose reaches the original rear surface later than the leading edge.

The mechanics of oblique impact are also more complex than normal impact (see Fig. 8) as bending waves as well as longitudinal waves are generated [37]. Consider first a hemispherical-nosed rod (see Fig. 8). The initial phase can be seen to be the ejection of plate material, mostly in the direction of impact. In Fig. 9, 'backward' ejection of material can be seen to cease after about 6–7 μs .

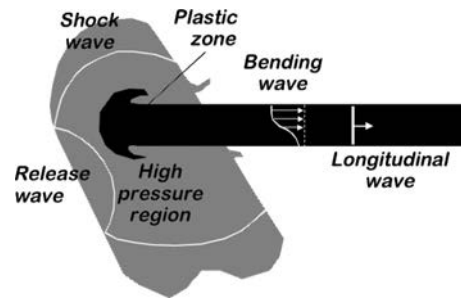


FIG. 8. Schematic diagram of wave phenomena due to ballistic impact of a rod on an angled target. Adapted from reference [18] p. 299.

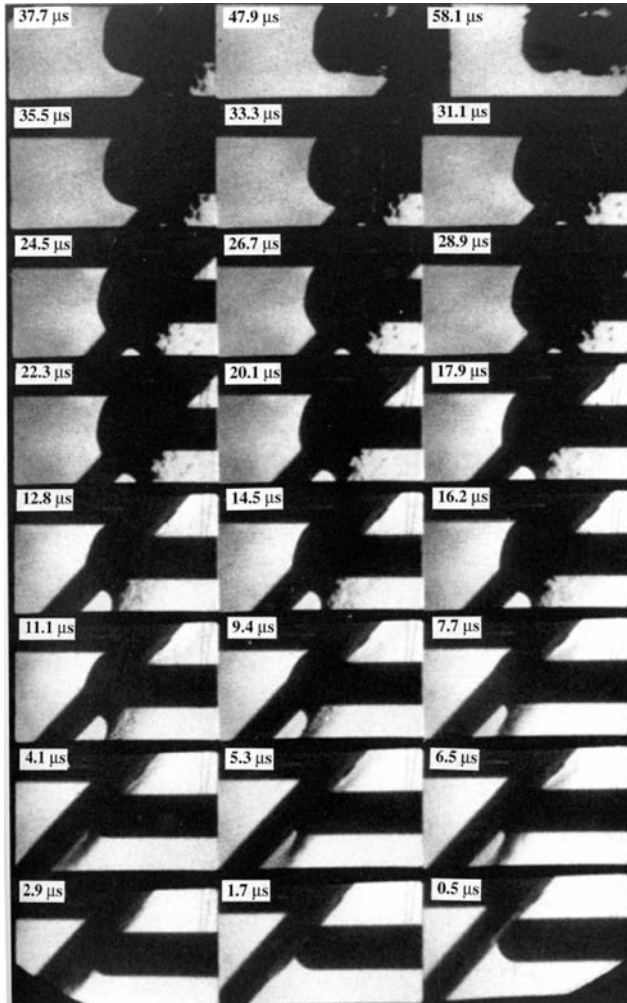


FIG. 9. High-speed photographic sequence of the impact of a 4.8 mm thick aluminium plate at 45° on a round-nosed copper rod at 830 m s^{-1} .

In this experiment, very little sliding of the rod on the plate took place and the rod started perforating the plate close to the impact point around $30\ \mu\text{s}$ after impact.

The craters due to oblique impact are usually symmetric in the plane. For small amounts of slip, they are oval in shape. For large amounts of slip, they have the form of long shallow grooves terminating where perforation occurs. Elongated craters are often associated with bending of the rod, raising the frictional forces between the rod and the plate. An example of this can be seen in Fig. 10 where the bulge can be seen moving at a constant velocity along the rear

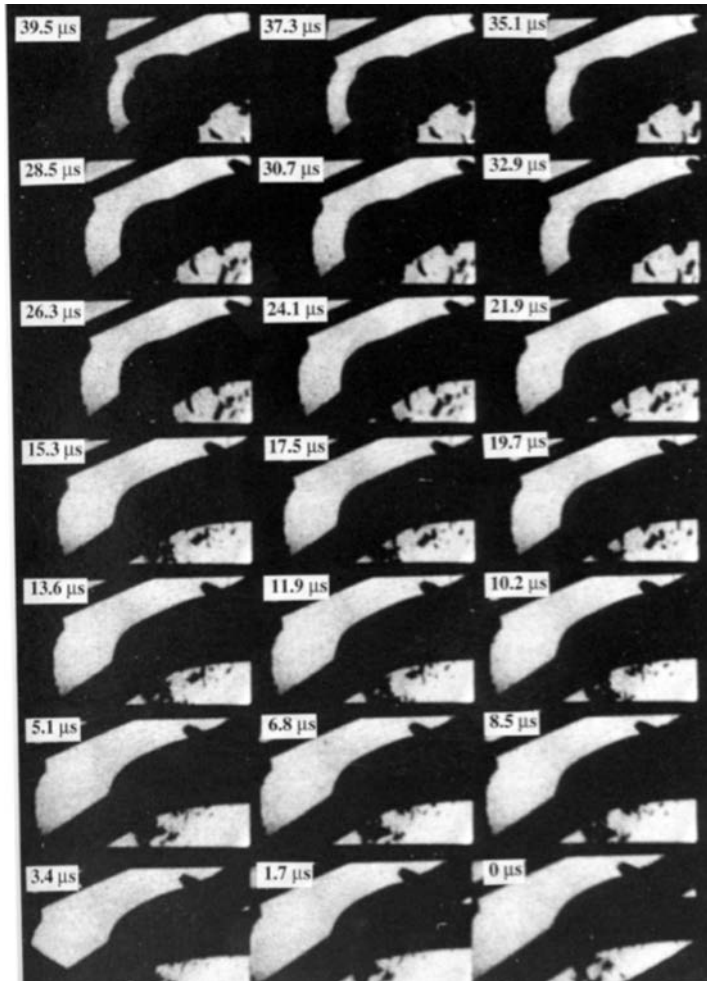


FIG. 10. Selected frames from the high-speed photographic sequence of the impact of a 5 mm thick RHA steel plate at 60° on a round-nosed tungsten alloy rod at $645\ \text{m s}^{-1}$. Note that in this sequence the time at which impact occurred is not known, so the first frame (bottom right) is set as time zero.

surface of the plate for some time before perforation finally occurred at around $35 \mu\text{s}$. This experiment was performed quite close to the ricochet angle.

For oblique impact it is not possible to predict where on the rear surface the bulge will first appear. Often it is laterally displaced beyond the projection of the rod cross-section. The resulting bulge subsequently lengthens along that surface back towards the rod axis and then past it and a plug of material will be pushed out as for normal impact.

Figure 11 presents a comparison at similar times between the oblique impact of round-nosed and flat-ended steel rods by 6 mm thick dural plates. The main difference is that the flat-ended rod produces a hinge of material in the target that breaks off as a few (possibly even one) large pieces (Fig. 11d) whereas the round-ended rod generates many small fragments in the dural plate (Fig. 11b).

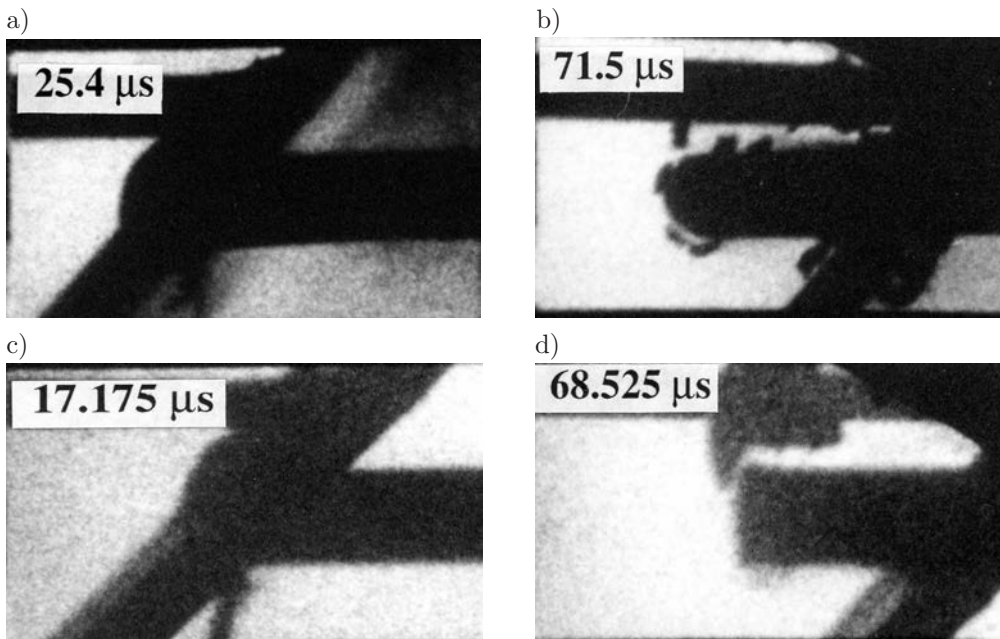


FIG. 11. Comparison of 45° oblique impact of two types of mild steel rods by dural plates: a) and b) impact conditions: 9.5 mm diameter, 215 mm long hemispherical-ended rod, 6 mm thick plate at 550 m s^{-1} ; c) and d) impact conditions: 9.5 mm diameter, 215 mm long flat-ended rod, 5.9 mm thick dural at 549 m s^{-1} .

Figures 12 and 13 show up some of the similarities and differences between the normal and oblique impact of dural plates on round-nosed mild steel rods with that of RHA steel plates on a tungsten rod at similar impact speeds. Recall that the reason for choosing the materials of the plate/penetrator pairs studied was that the ratios of density and yield strength were similar to RHA/tungsten (see Table 2). It can be seen from Fig. 13 that the RHA plate produces larger

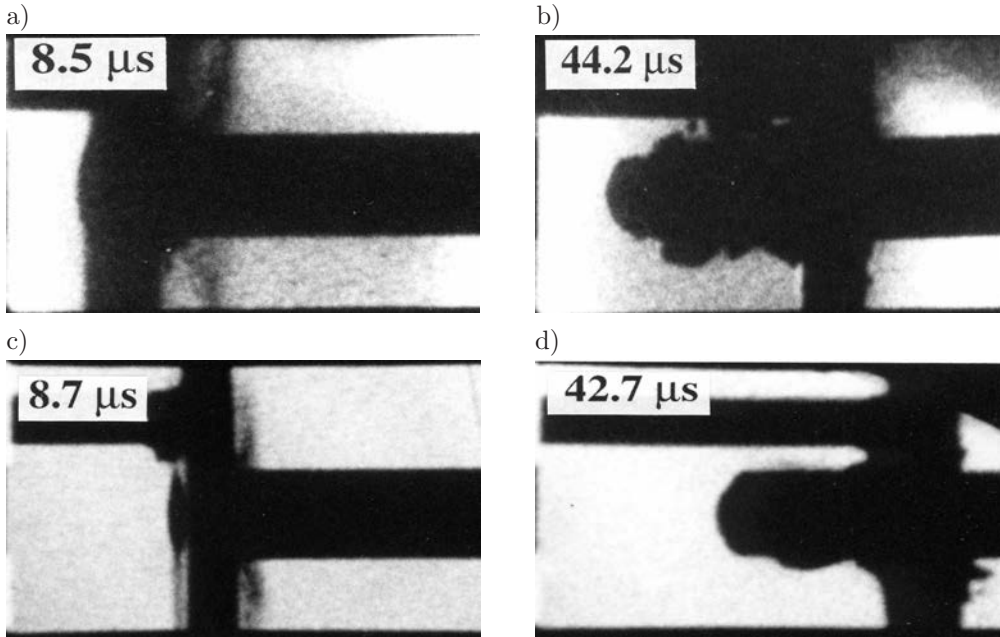


FIG. 12. Comparison of images taken at similar times after normal impact from high speed photographic sequences of the impact of 9.5 mm diameter mild steel rod by a 6 mm thick dural plate at 555 m s^{-1} (frames a) and b)) and a 10 mm diameter tungsten alloy rod by a 5 mm thick RHA steel plate at 533 m s^{-1} (frames c) and d)).

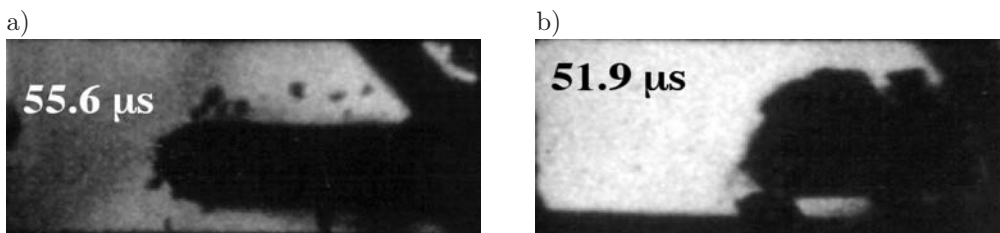


FIG. 13. Comparison of the impact of (a) a 5.9 mm thick dural plate against a 9.5 mm diameter, 215 mm long round-nosed mild steel rod at 823 m s^{-1} , 45° impact angle; b) a 5 mm thick RHA steel plate against a 10 mm diameter, 100 mm long round-nosed tungsten alloy rod at 810 m s^{-1} , 45° impact angle.

fragments than the dural. It was also observed that the tungsten rods deformed more than the mild steel rods and sometimes shattered, particularly in oblique impact. Both RHA and tungsten are more brittle than either dural or mild steel. So although dural/mild steel experiments can provide information useful to the RHA/tungsten problem, there are important differences particularly with respect to rod deformation and fracture of both target and penetrator. The main advantage of using mild steel and dural in preliminary experiments is that these materials are much cheaper and more readily available. Such experiments can

provide an indication of expected events along with timings and outcomes of various geometries. They can also provide useful results before committing to more expensive, full-scale experiments [22].

Considering the other pair of metals studied (aluminium/copper), we see from Fig. 14 that the main visual difference is that the aluminium deforms without fracture to much larger strains than mild steel (compare Figs. 14b and 14d). Copper and aluminium also strain-harden much more than the other pairs of materials considered. The impact stresses (normalised by the plate yield stress) for the impact velocities studied were largest for the aluminium/copper pair, ranging from 32–53. Those for dural/mild steel ranged from 20–30 and that for RHA steel/tungsten ranged from 8–14. Thus we conclude that the aluminium/copper combination is less useful for performing cheaper preliminary studies of RHA steel/tungsten impacts than dural/mild steel.

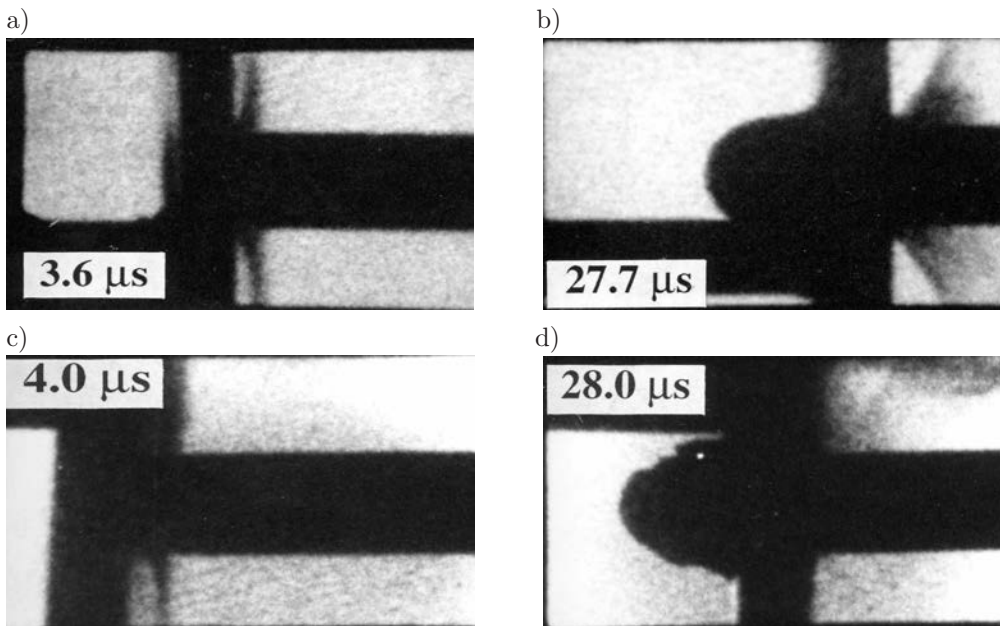


FIG. 14. Comparison of selected frames from a high-speed photographic sequence taken of the normal impact between a 4.8 mm thick pure aluminium plate and a 10 mm diameter, 99 mm long annealed round-nose copper rod at 549 m s^{-1} (frames a) and b)) with those at similar times (frames c) and d)) from the impact of a 6 mm thick dural plate on a 9.5 mm diameter, 215 mm long round-nosed mild steel rod at 554 m s^{-1} .

4. IMPACT INSTRUMENTATION

In order to decide what instrumentation to use, it is necessary first to consider what stress-wave activity we might expect. On first impact, shock waves are

launched into both the rod and the plate [38]. For a flat-ended rod struck by a plate at normal incidence, those two waves are both initially planar. For other geometries the shock structures are more complex. Behind the shock wave in the rod, material flows plastically. Rarefaction waves also travel inwards from the free surfaces modifying the shock structure and sometimes producing internal fractures [39]. Elastic compression and shear waves meanwhile run ahead of the plastic deformation front and reflect from any free surfaces they encounter.

As the stationary rod penetrates the moving plate, both the rod and plate deform plastically. The stress at the boundary of the rod and the plate has the effect of accelerating material within the rod up towards the velocity of the impacting plate (Fig. 15). As this happens, the stress at the rod-target interface decreases. When this drops below the flow stress, the rod starts to behave rigidly. As the rod nears the rear surface of the plate, a bulge appears. A plug may also form if the plate material is susceptible to ASB formation. When removed from the constraint of the surrounding material, the plug may detach as a solid disc or fracture into pieces, depending upon the plate thickness, ductility and strain-to-failure etc. Blunting of the projectile nose is common. In addition, plastic distortion may reach some considerable distance back into the rod.

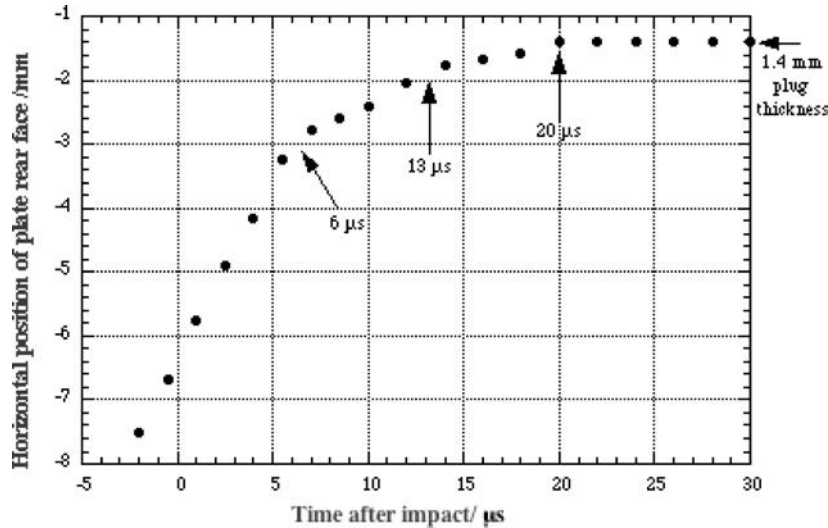


FIG. 15. Plot of the rear surface of a 3 mm thick dural plate impacted normally by a 9.5 mm diameter mild steel rod at 554 m s^{-1} . Data were measured from the high-speed photographic sequence taken. Visible plate bulging began around $6 \mu\text{s}$.

Stress wave effects due to plate penetration and perforation make the rod response more complex than in Taylor impact (Fig. 16). However, as in Taylor impact, an elastic wave propagates to the end of the rod and returns to interact repeatedly with the plastic front (Fig. 17), lowering the stress in the process.

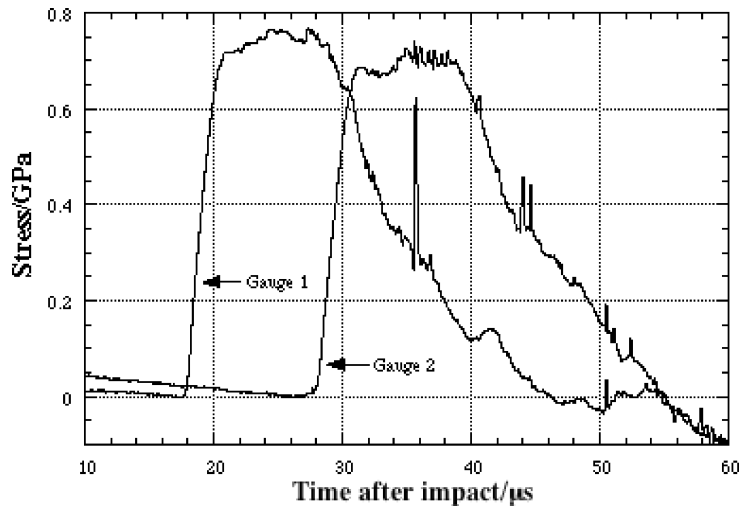


FIG. 16. Stress pulses from manganin pressure gauges embedded in a round-nosed mild steel rod impacted by a 6 mm thick dural plate at 554 m s^{-1} .

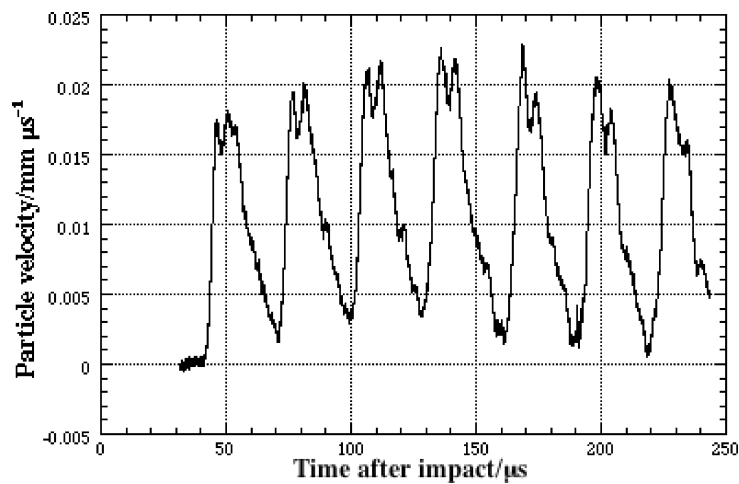


FIG. 17. VISAR trace for the rear of a round-nosed mild steel rod impacted by a 6mm thick dural plate at 554 m s^{-1} .

Because of the complexity associated with interpreting waves in rods generated by the impact and perforation of thin metal plates, some instrumented experiments were performed using thin alumina plates (Fig. 18). These plates maintain a high stress on the end of the rod for a relatively long period of time producing a more flat-topped stress pulse allowing the effects of elastic wave dispersion to be assessed without the complexities introduced by early perforation. Such experiments also allow the high rate, low strain mechanical properties of the mild steel rods to be determined [40, 41].

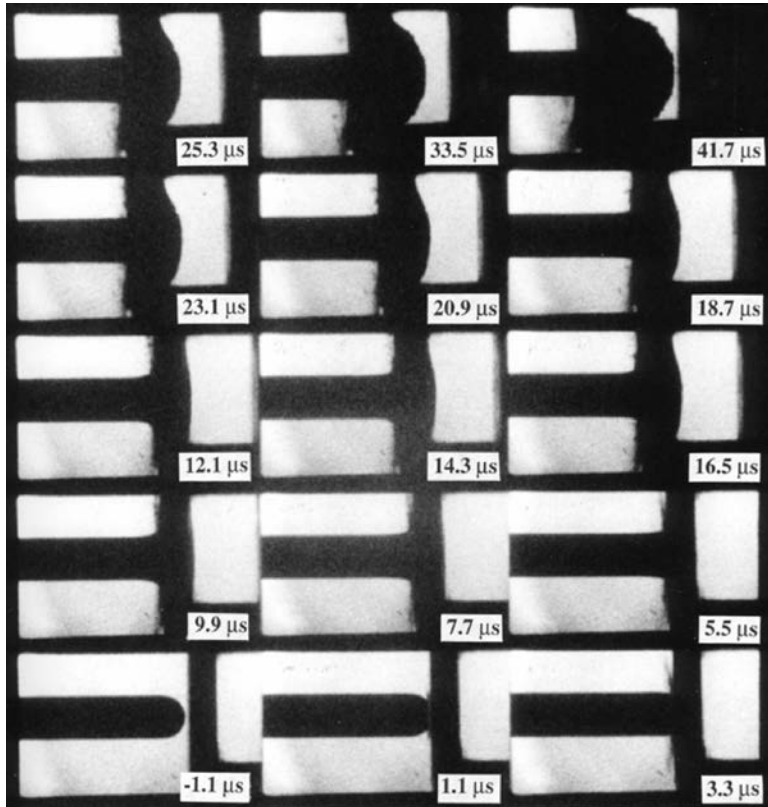


FIG. 18. High speed photographic sequence of the normal impact of a 9.5 mm diameter round nosed mild steel rod by a 6.5 mm thick alumina plate moving from right to left at 525 m s^{-1} .

Elastic wave dispersion in rods is well-known not only to reduce the slope of the rise up to maximum stress but also to introduce oscillations into the measured signal. The major source of distortion is that the velocity of stress waves in rods depends upon frequency. These effects were shown by both POCHHAMMER [42] and CHREE [43] to be intrinsic to infinitely long, but finite diameter, rods. They are, therefore, not artefacts specific to rods of finite length. However, dispersion is considerably more complicated for finite-length rods and generally agreed to be mathematically intractable [44].

Three experiments were performed, two with hemispherical-nosed ends and one with flat. Figure 19 presents the two stress gauge traces produced by the impact on a round-nosed steel rod of a 3 mm thick alumina plate moving at $541 \pm 5 \text{ m s}^{-1}$ and mounted directly on the front of the sabot. The underlying slew rate of the gauge power supply can be seen as a negative slope before the arrival of the pulses. The time of impact was determined to an accuracy of $\pm 0.7 \mu\text{s}$ from the high-speed photographic sequence taken.

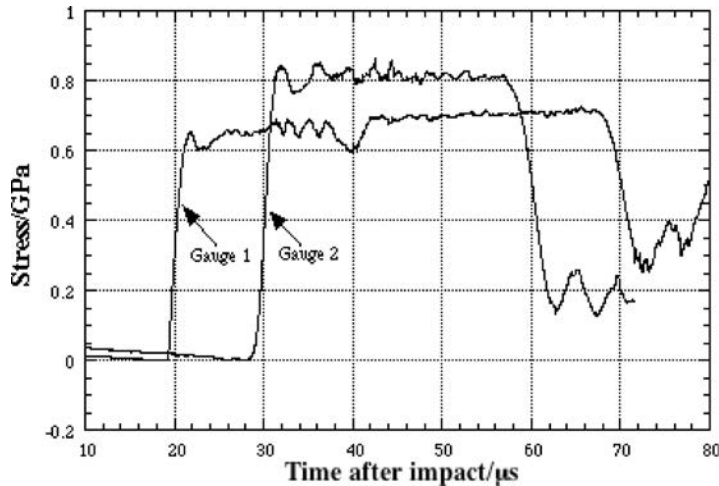


FIG. 19. Stress pulses recorded by two manganin stress gauges located at 90 mm (gauge 1) and 140 mm (gauge 2) from the impact point of a 9.5 mm diameter, 215 mm long round-nosed mild steel rod struck by a 3 mm thick alumina plate mounted on the front surface of a polycarbonate sabot and travelling at 541 m s^{-1} .

The stress can be seen to rise up to an initial overshoot followed by a ‘plateau’ region with some oscillations. These oscillations are due to dispersion and therefore do not occur at the impact face. They are, however, real at the gauge location and not an artefact of the gauges. The stress pulses end when the tensile release wave from the rear of the rod reaches the gauge locations. The time from the start of the rise until the start of the decay gives a measure of the velocity of the fastest elastic wave in the rod. The wave velocity calculated in this way was 5200 m s^{-1} for the signal from gauge 1 and 5170 m s^{-1} for the signal from gauge 2 which agree very well with the value of 5200 m s^{-1} measured using an acoustic wave generator. The velocity calculated from the transit time between the two gauges was 5520 m s^{-1} , 5% different to the other values.

Note that in this particular experiment there was a discrepancy in the maximum stress reached that was greater than the variation in the gauge factor (typically 2%). Gauge 1 recorded a stress of 0.65 GPa at the end of the rising phase creeping up to 0.70 GPa by the end of the pulse, whereas gauge 2 recorded a stress rising directly to 0.80 GPa. It is not known why this was so and this difference was not seen in other experiments (see, for example, Fig. 20).

The rise time for the pulse recorded by gauge 1 was $2.1 \mu\text{s}$ and that for gauge 2 was $3.1 \mu\text{s}$. These times are in reasonable agreement with the $4 \mu\text{s}$ rise time measured by ROSENBERG and BLESS [41] at a distance of 127 mm along mild steel rods impacted at about half this velocity. Dispersion sets a lower limit to the rise time and depends upon the distance the pulse has travelled along the rod (see Fig. 21).

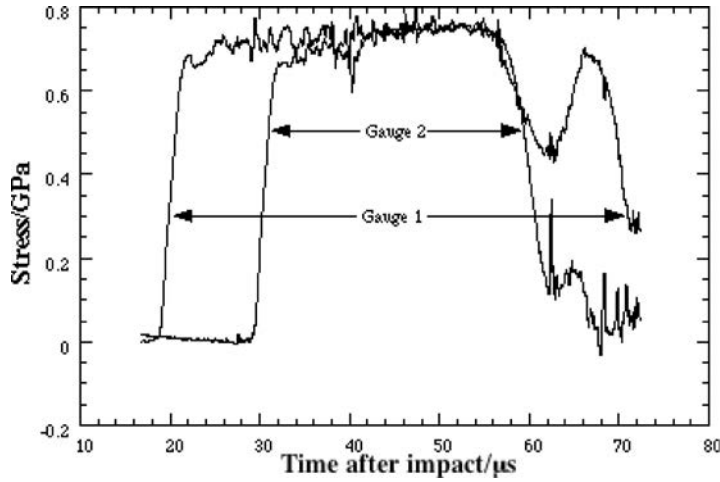


FIG. 20. Stress pulses recorded by two manganin stress gauges located at 90 mm and 140 mm from the impact point of a 9.5 mm diameter, 215 mm long round-nosed mild steel rod by a 6.5 mm thick alumina plate mounted on pillars on a polycarbonate sabot travelling at 525 m s^{-1} .

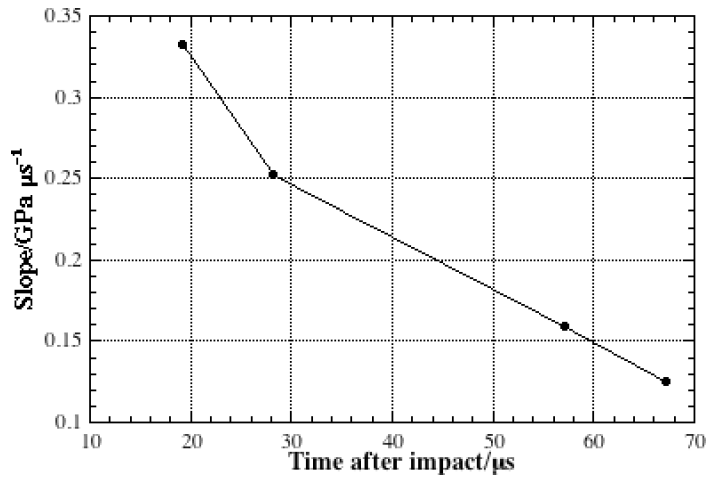


FIG. 21. Graph of the gradients of the rise and decay portions of the stress pulses shown in Fig. 19 versus time from impact.

A VISAR measurement (see Fig. 22) was also performed on the rear end of the rod. This trace confirms many features of the stress pulses shown in Fig. 19. The velocity can be seen to rise to $0.033 \text{ mm } \mu\text{s}^{-1}$, equivalent to 0.66 GPa using the following relation:

$$(4.1) \quad \sigma = 0.5\rho cv,$$

where ρ is the density, c is the elastic wave speed of mild steel (see Table 1) and v is the particle velocity.

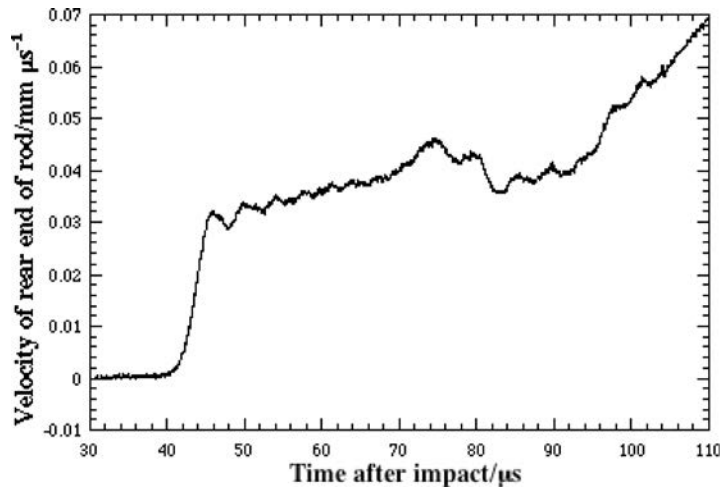


FIG. 22. VISAR trace recorded at the rear end of the round-nosed mild steel rod impacted by a 6.5 mm thick alumina plate at 525 m s^{-1} (same impact as Figs. 18 and 20).

The initial rising slope is $0.009 \text{ mm } \mu\text{s}^{-2}$, equivalent to $0.18 \text{ GPa } \mu\text{s}^{-1}$. This value lies between those for the two rises (0.28 and $0.30 \text{ GPa } \mu\text{s}^{-1}$) and the two decays (both $0.16 \text{ GPa } \mu\text{s}^{-1}$) recorded by the stress gauges, consistent with the fact that the pulse reached the end of the rod midway between the rise and decay of the stress recorded at gauge 2. Since the loading at the impact face continues for an extended period, the velocity of the rear of the rod does not decrease during the course of the trace presented in Fig. 22, rather the velocity creeps up steadily from the top of the initial rise. Then, there is a slight peak followed by a dip of short-duration at around $80 \mu\text{s}$ after which the velocity rises again. This peak occurs close to the time it would take for the elastic wave to return from the rear of the rod to the location of gauge 2. So the dip may represent a partial release of the gauge package. The velocity eventually rises significantly beyond that expected on the basis of the stress gauge readings. This may be due to the rear of the rod approaching the position of the duplex optical fibre which brings laser light to and from the VISAR. As this happens, the VISAR system compensates for the change in intensity of the beam reflected from the rod, losing accuracy in the process.

The high-speed photographic sequence for this experiment (Fig. 18) confirms the relatively long time that the alumina plate resisted penetration. During this time the front of the rod can be seen to deform plastically and increase in diameter (see, for example, the frame labelled $5.5 \mu\text{s}$). Note also the jetting of material visible about $3 \mu\text{s}$ into the impact. The angle of jetting is similar to that for a ductile plate at about the same time (see Fig. 23), though as penetration proceeds, the angle of jetting increases for a ductile material (Fig. 23d).

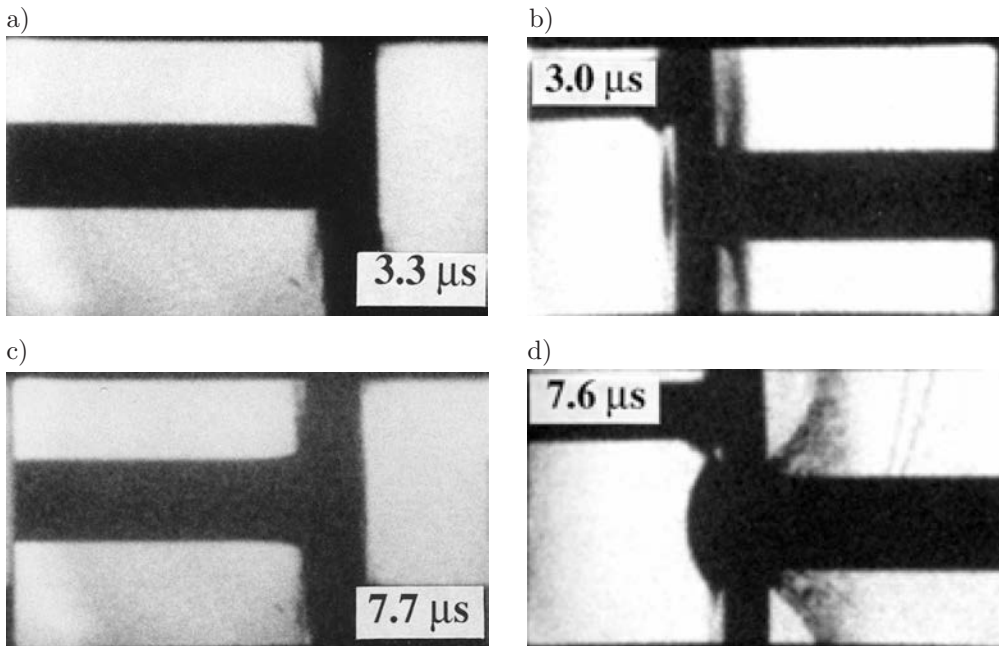


FIG. 23. Comparison of impacts at similar times on a rod by (a) and (c) – an alumina plate and (b) and (d) – a metal plate. Experimental conditions: a) and c) 9.5 mm diameter round-nosed mild steel rod, 6.5 mm thick alumina plate moving from right to left at 525 m s^{-1} ; b) and d) 10 mm diameter round-nosed copper rod, 4.8 mm thick aluminium alloy plate, moving from left to right at 855 m s^{-1} .

Apart from the direct photographic evidence the rod deforming laterally between about 5 and 10 μs into the impact (Fig. 23c), there is also indirect evidence of rod deformation in that the position of the plate rear surface at the end of the high-speed sequence (41.7 μs ; not shown) is actually to the left of the initial point of the rod nose by more than 1 mm, implying a negative thickness for the ceramic material pushed ahead of the rod. However, if the double transit time of the elastic wave in the rod (41.5 μs) is taken into account, the rod would only just have begun to move bodily by this point. Thus, the rod must have shortened. Another piece of evidence for this is that the time measured from the photographs for the bulge to protrude a distance equal to a single plate thickness is 25.3 μs . The implication of this is that the rear of the plate took the same time to move out to one plate thickness as the rod would have done had it been unimpeded, yet there appears still to be plate material ahead of the rod. But since the rod had not yet begun to accelerate bodily, the rod must have shortened.

The third experiment in this series involved firing a 6.5 mm thick alumina plate (mounted on rods) at 523 m s^{-1} against a flat-ended mild steel rod. Figure 24 presents the two resulting stress gauge traces along with the VISAR data

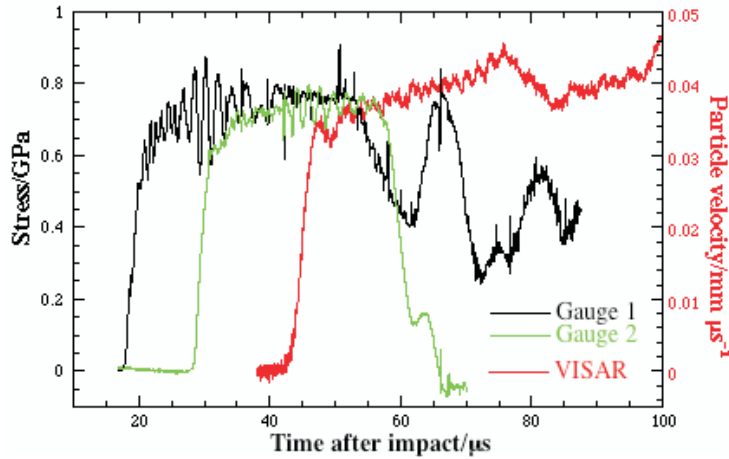


FIG. 24. Stress pulses recorded by two manganin stress gauges located at 90 mm and 140 mm from the impact point of a 9.5 mm diameter, 215 mm long flat-ended mild steel rod along with the particle velocity of the far end of the rod measured using VISAR. The rod was impacted by a 6.5 mm thick alumina plate mounted on pillars on a polycarbonate sabot travelling at 523 m s^{-1} .

plotted on the same time axis. It is noticeable that the pulse from gauge 1 also shows the same break in the plateau stress at approximately the same time as for the second shot against a round-nosed rod (see Fig. 20). The stress oscillations are of much greater amplitude in these traces compared to those in the round-nosed rod, particularly for gauge 1. Only the highest frequencies, with reduced amplitude, are still seen by gauge 2. The periods of these oscillations have values that are both longer and shorter than the time taken for an elastic wave to traverse the rod diameter once ($1.8 \mu\text{s}$).

The technique of impacting a long rod with a strong target provides a method of measuring the elastic wave amplitude under conditions of one-dimensional stress at strain rates of 10^2 – 10^3 s^{-1} and small strains. The data generated is therefore more directly comparable to plate impact (strain rates in excess of 10^5 s^{-1}) than that obtained from the split Hopkinson pressure bar (SHPB) which is normally used for the 10^3 – 10^4 s^{-1} strain rate regime. The other major difference between the SHPB and plate impact is that the SHPB can only be used to measure flow stresses in one-dimensional stress for plastic strains greater than about 5% [45] whilst plate impact gives the yield stress under one-dimensional strain (the Hugoniot elastic limit or HEL). This can make it difficult to compare results from the two techniques in rate dependent or work-hardening materials. We found the rod technique worked best using thin alumina plates and round-nosed rods since a flat-ended rod (equivalent to reverse Taylor impact) produces a stress pulse with higher amplitude oscillations (compare Fig. 20 and 25). In the light of the above considerations, all the rods were instrumented

by embedding manganin foil stress gauges within them 90 mm from the nose (gauge 1). For the longer steel rods, additional gauges were placed 140 mm from the nose (gauge 2).

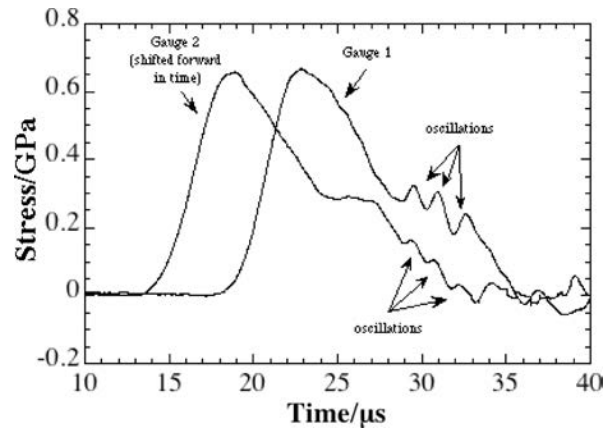


FIG. 25. Plot of the outputs of the manganin gauges located 90 and 140 mm from the impact point of a round-nosed mild steel rod struck by a 3mm thick dural plate at 556 m s^{-1} . The traces have been time-shifted so that the oscillations on the descending part of the pulses coincide in time.

For accurate measurement of the stress, the epoxy layer used to embed the gauge must be thin enough that the stress in the gauge package ‘rings up’ in a small fraction of the timescale of the experiment. Also the gauge must be positioned sufficiently far from the impact end so that three-dimensional end effects have died away. Ten rod diameters have been found to be sufficient [27, 44]. This was confirmed by modelling results (presented later in this paper in Figs. 29 and 30) which showed that in most cases the stress profile equilibrates by a distance equal to nine diameters of travel. Time-shifting the traces obtained from gauges placed at different positions in the rods shows that the oscillations travel at a lower speed than the bulk of the stress wave, and, hence, appear at a later stage of the pulse recorded from gauge 2 (Fig. 25).

Checks were also made both on the reproducibility and accuracy of the gauges. Reproducibility was checked by repeating experiments (Fig. 26). Accuracy was checked by comparing the gauge trace with the output of a VISAR (Fig. 27). As agreement was found to be satisfactory, most experiments were performed with gauges only as this is easier to do.

A check was also made of the amount of lateral strain at the first gauge location (nine bar diameters from the impact point) by replacing the stress gauge at that point in one experiment by a constantan foil strain gauge. The maximum strain recorded was only 0.17%, which is sufficiently small to imply that lateral strain has a negligible effect on the output of the stress gauges.

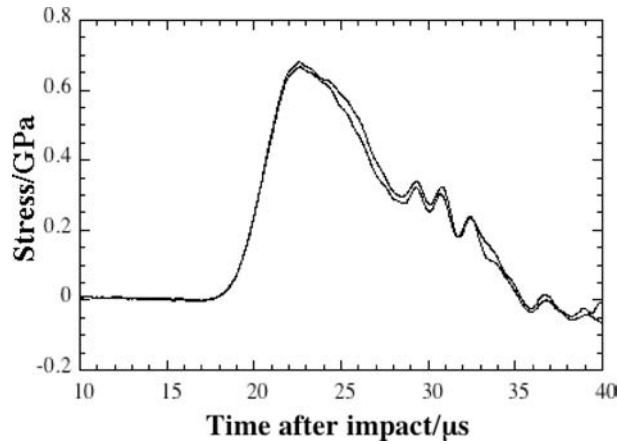


FIG. 26. Demonstration of the reproducibility of outputs of manganin gauges located 90 mm from the impact points of two round-nosed mild steel rods impacted by 3 mm thick dural plates at 556 and 561 m s^{-1} .

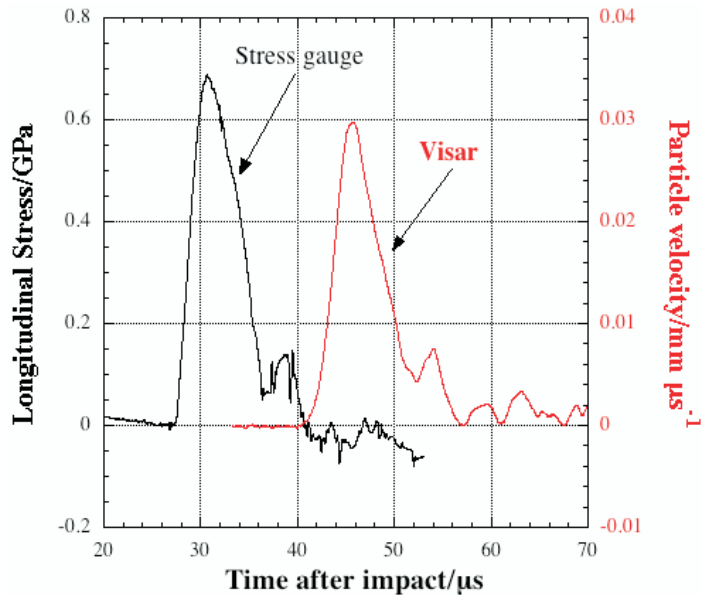


FIG. 27. Comparison of the output of the manganin stress gauge at location 2 with VISAR from the end of the rod for the impact of a 9.5 mm diameter round-nosed mild steel rod by a 3 mm thick dural plate at 835 m s^{-1} .

5. MODELLING OF TUNGSTEN RODS PERFORATING RHA PLATES

A modelling study of some of the round-nosed tungsten rod impacts on 5 mm thick RHA steel plates was performed using the second generation Eulerian hydrocode GRIM, which was developed by researchers in QinetiQ in order to

investigate general problems in explosive technology and penetration mechanics [46–50]. This hydrocode is capable of multi-material interaction in both 2D and 3D.

Three experiments were chosen for modelling: two at normal impact, 533 m s^{-1} (shot 41) and 833 m s^{-1} (shot 42), and one at 45° , 810 m s^{-1} (shot 46). The two normal impacts were treated as two-dimensional axisymmetric problems, whereas the oblique shot required three-dimensional treatment. The Zerilli-Armstrong (ZA) constitutive models (modified for the temperature variation of shear modulus) were used for the two materials (Eq. (5.1) and Table 5):

$$(5.1) \quad \sigma = (C_0 + C_1 \varepsilon^n) \mu_T / \mu_{293} + C_2 \exp(-C_3 T + C_4 T \log(\partial \varepsilon / \partial t)),$$

where C_0 to C_4 and n are constants and σ , ε , $\partial \varepsilon / \partial t$ and T are respectively stress, strain, strain rate and absolute temperature, μ_{293} the shear modulus at 293 K and μ_T the shear modulus at the current temperature. The constants were directly measured from interrupted tensile tests and are obtained by rearranging Eq. (5.1) and calculating slopes and intercepts. The modified Armstrong-Zerilli model was run in conjunction with a Mie-Grüneisen equation of state to describe the hydrostatic response.

Table 5. Parameters of the modified Armstrong-Zerilli constitutive model for the RHA steel and tungsten alloys used.

Parameter	FNC tungsten	RHA steel
Shear modulus [GPa]	13.4	9.545
C_0 [MPa]	600	780
C_1 [MPa]	750	715
C_2 [MPa]	2700	950
C_3 [K^{-1}]	0.0043	0.0052
C_4 [K^{-1}]	0.00017	0.00026
n	0.65	0.65

The rods that supported the plates (see Fig. 2) were not included in the simulations. Any influence of the plate mounts on the impact cannot occur until approximately $7 \mu\text{s}$ after impact since they are located 10 mm from the plate centre and an elastic double-wave transit of 20 mm in RHA steel takes $6.8 \mu\text{s}$. This would be seen at the gauge position some $25 \mu\text{s}$ or more after impact, just after the peak stress. Their influence on the measured signal is likely to be minor.

A mesh resolution study involving three mesh sizes of 1 mm, 0.5 mm and 0.25 mm was performed for each experiment to ensure that convergence was achieved.

The simulation technique was first used to calculate the axial stress in the rod at a Lagrangian gauge position 90 mm from the rod end corresponding to the measurements taken at gauge location 1 (Fig. 28). The simulated peak stresses can be seen to match the experiments quite well (~ 0.95 GPa), being most similar to shot 46, but a little higher than the mean stress of 0.88 GPa.

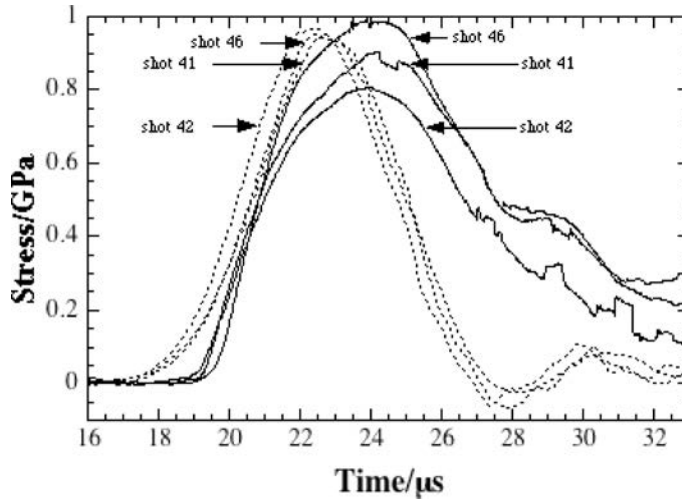


FIG. 28. Comparison of modelling with experiment for the output of manganin stress gauges 90 mm from the impact end for three hemispherical-ended 10 mm diameter tungsten rods impacted by 5 mm thick RHA steel plates. The solid lines are the experimental results; the dotted lines are the simulations. Experimental conditions: shot 41: normal impact, 533 m s^{-1} ; shot 42: normal impact, 833 m s^{-1} ; shot 46: 45° , 810 m s^{-1} .

The elastic wave velocity used in the model was determined from ultrasonic measurements on a plate made from the same tungsten alloy. This value appears to be a little higher than the elastic wave velocity in the rod, leading to a slightly early arrival (about $2 \mu\text{s}$) of both the compression wave and subsequent release wave, and thus to shorter pulse durations. The simulations also show more gradual and prolonged rises at the start, and the experiments exhibit more gradual ends to the rising phase. However, the maximum rates of stress rise are similar in both the simulations and experiments, indicating wave dispersion has been modelled quite well. The simulated pulses are more symmetrical with time than the experimental ones, but then the latter appear disturbed and noisy after about $27 \mu\text{s}$ and are, hence, probably unreliable after this, so the experimental pulse shape is not certain after this time.

However, unlike gauges, modelling can give information about the stresses at many points within the rod. Figure 29 shows the predicted stress distribution within the rod and plate for shot 41 for three times after impact. The top section of each frame is the simulation corresponding in time to the frames selected

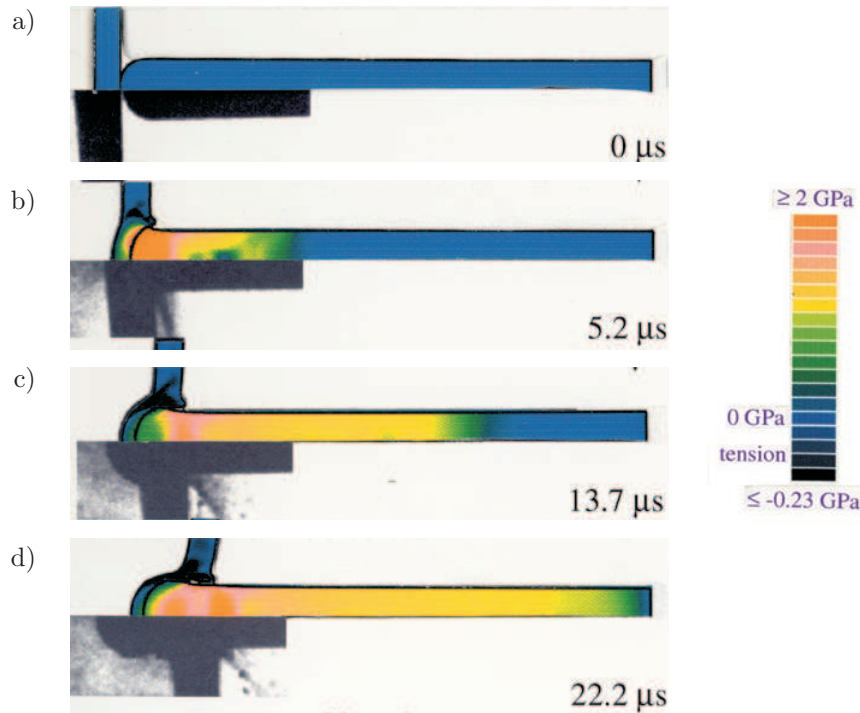


FIG. 29. Comparison of the simulated and experimental rod profiles of shot 41 (round-nosed tungsten alloy rod impacted normally by 5 mm thick RHA steel plate at 533 m s^{-1}). The colours indicate the stress levels (key given in right part of figure).

from the high-speed photographic record (bottom section). Only part of the rod lengths is shown. The elastic wavefront structure can be seen to become more planar in each successive frame and appears to be almost flat in profile by nine diameters (the location of gauge 1). As may be seen from Fig. 23, the high-speed photographs show the plate obliquely. Hence, the plate appears thicker than it truly is.

Note that when making a visual comparison between experiment and simulation the rear face of the plate can be seen in the photographs presented in frames (a) and (b). Note also that jetting of material was not incorporated in the simulation. The simulation overestimated the penetration time, probably because failure by ASBs and fracture was not incorporated. The simulation also overpredicted the extent of plate dishing (see particularly frame (d)). The reason failure mechanisms were not incorporated in the modelling was that the aim was to compare the simulations with the experimentally determined deformation of the rod and plate at early times. Since the Euler codes feature more than one material in a cell, then a manifestation of failure can be observed when the volume of the material falls below a set tolerance level in that cell.

Figure 30 presents a similar comparison between experiment and modelling for an oblique impact experiment (shot 46). One obvious difference to the normal impact case is the complexity of stress wave activity close to the nose of the rod even at short times. However, the stress wave again settles down to a more planar shape by the position of the first gauge location giving confidence that the stress pulses were recorded accurately. By frame (d) the elastic wave has returned to the nose, reflected, and is travelling back towards the rear a second time. In frames (b) and (c) the stress in the plate has concentrated on one side of the rod. Also the rod has flattened asymmetrically. However, by frame (d) the rod has self-sharpened. RECHT [51] suggested that deformed rods typically shear off material so that their final diameter is no greater than 125% of the original. Again the simulation predicts a faster penetration than actually occurred, though much of the detail as to what is going on is hidden by debris in the photographic sequences.

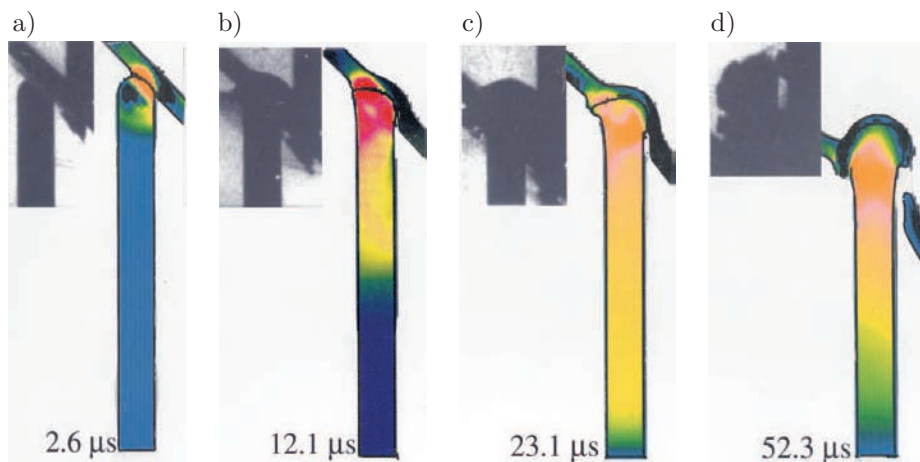


FIG. 30. Comparison of the simulated and experimental rod profiles of shot 46 (round-nosed tungsten alloy rod impacted at 45° by 5 mm thick RHA steel plate at 810 m s^{-1}). The same colour coding of stress was used as for Fig. 29.

To summarise, modelling is invaluable for giving insight into wave structures within the rod whereas experiments aid in ‘tuning’ the parameters of the constitutive model. They thus complement each other well.

6. CONCLUSIONS

Small-scale reverse ballistics experiments proved their worth in allowing the use of a wide range of diagnostics such as stress gauges, high-speed photography, and velocity interferometry (VISAR). These diagnostics provided a great

deal of information about plate perforation mechanisms. As the real materials used on the battlefield (RHA steel and tungsten) are expensive, we performed a study where less expensive pairs of materials with similar ratios of density and yield stress to determine whether these could be used in preliminary experiments to study the phenomenology of impact. We found that the less expensive materials were more ductile. Hence, the fracture behaviour of the real materials was not reproduced well, particularly in oblique impact. Even so, we found that the cheaper experiments can provide useful results before committing to more expensive, full-scale trials.

We also confirmed that it is possible to use stress gauges embedded in rods to measure dynamic mechanical properties of materials at low strains and at strain rates of between 10^2 and 10^3 s^{-1} . We found this was best done using thin ceramic plates and round-nosed rods. The patterns in the stress pulses often allow the impact parameters to be inferred as does high-speed photography of plate bulging or the deformation of in-plane grids. The results of stress gauge measurements were confirmed to be reproducible by performing repeat experiments and to be accurate by using VISAR. VISAR has a number of advantages over gauges in that it is more sensitive to low stress levels, has a faster response time, and can measure tensile release as well as compression. Dispersion of elastic waves affects both methods of measurement. Stress gauges are, however, cheaper and easier to use. They can also detect the exact time of impact if an electric pulse is given out by the impact process.

The numerical modelling that was performed confirmed the importance of including fracture if a predictive capability is required. This was particularly true for oblique impacts.

ACKNOWLEDGMENT

The research reported in this paper was funded by the British Ministry of Defence. We would like to thank Dr I.G. CULLIS for providing guidance and computer modelling expertise. We would also like to thank past and present members of the Cavendish Laboratory's mechanical and electronic workshops for assistance with the design and construction of apparatus and specimens required for these experiments. LCF was supervised initially by Dr (now Professor) N.K. BOURNE and then by Professor J.E. FIELD and Dr W.G. PROUD.

REFERENCES

1. M. E. BACKMAN, W. GOLDSMITH, *The mechanics of penetration of projectiles into targets*, Int. J. Engng. Sci., **16**, 1-99, 1978.
2. M. F. ASHBY, *A first report on deformation-mechanism maps*, Acta Metall., **20**, 887-898, 1972.

3. W. GOLDSMITH, S. A. FINNEGAN, *Penetration and perforation processes in metal targets at and above ballistic limits*, *Int. J. Mech. Sci.*, **13**, 843–866, 1971.
4. S. G. GRANTHAM, H. T. GOLDREIN, W. G. PROUD, J. E. FIELD, *Digital speckle radiography: A new ballistic measurement technique*, *Imaging Sci. J.*, **51**, 175–186, 2003.
5. L. C. FORDE, W. G. PROUD, S. M. WALLEY, P. D. CHURCH, I. G. CULLIS, *Ballistic impact studies of a borosilicate glass*, *Int. J. Impact Engng.*, **37**, 568–578, 2010.
6. J. I. BLUHM, *Stresses in projectiles during penetration*, *Proc. Soc. Exptl. Stress Analysis*, **13**, 2, 167–182, 1955.
7. L. M. BARKER, R. E. HOLLENBACH, *Laser interferometer for measuring high velocities of any reflecting surface*, *J. Appl. Phys.*, **43**, 4669–4675, 1972.
8. T. W. BURKE, W. F. ROWE, *Bullet ricochet: A comprehensive review*, *J. Forensic Sci.*, **37**, 1254–1260, 1992.
9. T. W. BJERKE, G. F. SILSBY, D. R. SCHEFFLER, R. M. MUDD, *Yawed long-rod penetration*, *Int. J. Impact Engng.*, **12**, 281–292, 1992.
10. R. L. LANDINGHAM, A. W. CASEY, *Final report of the light armor program*, Report no. UCRL-51269, Livermore, CA, Lawrence Livermore Laboratory, 1972.
11. H.-J. ERNST, K. STERZELMEIER, T. WOLF, R. NÜSING, *Reactive armor mechanisms against KE-threat: High explosives and electromagnetic forces*, [in:] *Proc. 17th Int. Symp. on Ballistics*, vol. 1, pp. 71–78, van Niekerk C. [Ed.], The South African Ballistics Organisation, Moreleta Park, South Africa, 1998.
12. G. BEN-DOR, A. DUBINSKY, T. ELPERIN, *On the ballistic resistance of multi-layered targets with air gaps*, *Int. J. Solids Structures*, **35**, 3097–3103, 1998.
13. G. BEN-DOR, A. DUBINSKY, T. ELPERIN, *Effect of air gap and order of plates on ballistic resistance of two layered armor*, *Theor. Appl. Fract. Mech.*, **31**, 233–241, 1999.
14. T. J. MOYNIHAN, J. C. LASALVIA, M. S. BURKINS, *Analysis of the shatter gap phenomenon in a boron carbide/composite laminate armor system*, [in:] *Proc. 20th Int. Symp. on Ballistics*, National Defense Industrial Association, pp. 1096–1103, Carleone J., Orphal D. [Eds.], Lancaster, PA, 2002.
15. Z. ROSENBERG, E. DEKEL, *The relation between the penetration capability of long rods and their length to diameter ratio*, *Int. J. Impact Engng.*, **15**, 125–130, 1994.
16. D. L. ORPHAL, R. R. FRANZEN, *Penetration mechanics and performance of segmented rods against metal targets*, *Int. J. Impact Engng.*, **10**, 427–438, 1990.
17. G. BIRKHOFF, D. P. MACDOUGALL, E. M. PUGH, G. I. TAYLOR, *Explosives with lined cavities*, *J. Appl. Phys.*, **19**, 563–582, 1948.
18. J. A. ZUKAS [Ed.], *High Velocity Impact Dynamics*, Wiley, New York, 1990.
19. Z. ROSENBERG, E. DEKEL, *Strength effects in long-rod penetration*, [in:] *Structures under Shock and Impact IV*, pp. 137–148, Jones N., Brebbia C.A., Watson A.J. [Eds.], Computational Mechanics Publications, Southampton, UK, 1996.
20. Z. ROSENBERG, E. DEKEL, *On the role of material properties in the terminal ballistics of long rods*, *Int. J. Impact Engng.*, **30**, 835–851, 2004.
21. T. BØRVIK, M. LANGSETH, O. S. HOPPERSTAD, K. A. MALO, *Ballistic penetration of steel plates*, *Int. J. Impact Engng.*, **22**, 855–886, 1999.

22. T. BØRVIK, S. DEY, O. S. HOPPERSTAD, M. LANGSETH, *On the main mechanisms in ballistic perforation of steel plates at sub-ordnance impact velocities*, [in:] Predictive Modeling of Dynamic Processes, pp. 189–219, Hiermaier S. [Ed.], Springer, Berlin, 2009.
23. P. C. CHOU, J. HASHEMI, A. CHOU, H. C. ROGERS, *Experimentation and finite element simulation of adiabatic shear bands in controlled penetration impact*, Int. J. Impact Engng., **11**, 305–321, 1991.
24. J. YU, X. DONG, J. ZHANG, *A study of adiabatic shear plugging in Ti6Al4V alloy*, Key Engng. Mater., **177**, 387–392, 2000.
25. Y.-W. LEE, T. WIERZBICKI, *Fracture prediction of thin plates under localized impulsive loading. 1: Dishing*, Int. J. Impact Engng., **31**, 1253–1276, 2005.
26. L. W. KENNEDY, O. E. JONES, *Longitudinal wave propagation in a circular bar loaded suddenly by a radially distributed end stress*, Trans. ASME: J. Appl. Mech., **36**, 470–478, 1969.
27. D. A. GORHAM, *Measurement of stress-strain properties of strong metals at very high strain rates*, Inst. Phys. Conf. Ser., **47**, 16–24, 1980.
28. L. C. FORDE, N. K. BOURNE, Z. ROSENBERG, R. CORNISH, N. J. LYNCH, I. G. CULLIS, P. D. CHURCH, *Experimental investigation and analysis of penetration in oblique impact*, [in:] Proc. 16th Int. Symp. on Ballistics, vol. 3, pp. 641–649, American Defense Preparedness Association, Arlington, Virginia, 1996.
29. N. K. BOURNE, Z. ROSENBERG, D. J. JOHNSON, J. E. FIELD, A. E. TIMBS, R. P. FLAXMAN, *Design and construction of the UK plate impact facility*, Meas. Sci. Technol., **6**, 1462–1470, 1995.
30. S. P. MARSH, *LASL Shock Hugoniot Data*, University of California Press, Berkeley, CA, 1980.
31. M. B. LESSER, *Analytic solutions of liquid-drop impact problems*, Proc. R. Soc. Lond. A, **377**, 289–308, 1981.
32. D. R. ANDREWS, J. E. FIELD, *The erosion of metals by the normal impingement of hard solid spheres*, J. Phys. D: Appl. Phys., **15**, 571–578, 1982.
33. J. E. FIELD, M. B. LESSER, J. P. DEAR, *Studies of two-dimensional liquid-wedge impact and their relevance to liquid-drop impact problems*, Proc. R. Soc. Lond. A, **401**, 225–249, 1985.
34. Y. L. BAI, B. DODD, *Adiabatic Shear Localization: Occurrence, Theories and Applications*, Pergamon, Oxford, 1992.
35. S. M. WALLEY, *Shear localization: A historical overview*, Metall. Mater. Trans. A, **38**, 2629–2654, 2007.
36. J. P. DEAR, *Use of high-speed photography in the evaluation of polymer materials*, Proc. SPIE, **1358**, 37–42, 1990.
37. W. G. PROUD, N. LYNCH, A. MARSH, J. E. FIELD, *Instrumented smallscale rod penetration studies: The effect of pitch*, [in:] Proc. 19th Int. Symp. on Ballistics, pp. 1289–1295, Crewther I.R. [Ed.], Interlaken, Switzerland, 2001.
38. G. R. WILLMOTT, D. D. RADFORD, *Taylor impact of glass rods*, J. Appl. Phys., **97**, 093522, 2005.

39. D. J. CHAPMAN, D. D. RADFORD, M. REYNOLDS, P. D. CHURCH, *Shock induced void nucleation during Taylor impact*, *Int. J. Fract.*, **134**, 41–57, 2005.
40. Z. ROSENBERG, S. J. BLESS, *Determination of dynamic yield strengths with embedded manganin gages in plate-impact and long-rod experiments*, *Exper. Mech.*, **26**, 279–282, 1986.
41. Z. ROSENBERG, S. BLESS, *Stress wave measurements in impulsively loaded long steel rods with embedded manganin gauges*, [in:] *Proc. Int. Symp. on Intense Dynamic Loading and its Effects*, pp. 742–746, Zheng Z., Ding J. [Eds.], Pergamon, Oxford, 1988.
42. L. POCHHAMMER, *Über Fortpflanzungsgeschwindigkeiten kleiner Schwingungen in einem unbegrenzten isotropen Kreiszyylinder*, *J. reine angew. Math.*, **81**, 324–336, 1876.
43. C. CHREE, *The equations of an isotropic elastic solid in polar and cylindrical coordinates: Their solution and application*, *Trans. Cambridge Philos. Soc.*, **14**, 250–369, 1889.
44. N. A. SAFFORD, *Materials testing up to 10^5 s⁻¹ using a miniaturised Hopkinson bar with dispersion corrections*, [in:] *Proc. 2nd. Int. Symp. on Intense Dynamic Loading and its Effects*, pp. 378–383, Zhang G., Huang S. [Eds.], Sichuan University Press, Chengdu, P.R. China, 1992.
45. G. T. GRAY III, *Classic split-Hopkinson pressure bar testing*, [in:] *ASM Handbook. 8: Mechanical Testing and Evaluation*, pp. 462–476, Kuhn H., Medlin D. [Eds.], ASM International, Materials Park, Ohio, 2000.
46. P. D. CHURCH, I. CULLIS, *Development and application of high strain rate constitutive models in hydrocodes*, *J. Phys. IV France*, **1**, (C3), 917–922, 1991.
47. P. D. CHURCH, T. ANDREWS, B. GOLDTHORPE, *A review of constitutive model development within DERA*, [in:] *Structures under Extreme Loading Conditions (PVP 394)*, pp. 113–120, Jerome D.M. [Ed.], American Society of Mechanical Engineers, New York, 1999.
48. E. C. CAMERON, D. C. BARTON, T. D. ANDREWS, P. D. CHURCH, *An experimental and numerical study of the ductile fracture process for rolled homogeneous armour alloy steel*, *J. Phys. IV France*, **10** (Pr. 9), 209–214, 2000.
49. L. C. FORDE, W. G. PROUD, S. M. WALLEY, *Symmetrical Taylor impact studies of copper*, *Proc. R. Soc. A*, **465**, 769–790, 2009.
50. L. C. FORDE, S. M. WALLEY, M. PEYTON-JONES, W. G. PROUD, I. G. CULLIS, P. D. CHURCH, *The use of symmetric Taylor impact to validate constitutive models for an fcc metal (copper) and a bcc alloy (RHA steel)*, [in:] *Proc. 9th Int. Conf. on the Mechanical and Physical Behaviour of Materials under Dynamic Loading (DYMAT 2009)*, pp. 1245–1250, EDP Sciences, Les Ulis, France, 2009.
51. R. F. RECHT, *Taylor ballistic impact modelling applied to deformation and mass loss determinations*, *Int. J. Engng Sci.*, **16**, 809–827, 1978.

Received January 5, 2011; revised version July 19, 2011.
